Supporting Information

Kato et al. 10.1073/pnas.1105848108

SI Materials and Methods

Analysis of High Mobility Group Nucleosomal (HMGN) 2-Nucleosome Binding Data. A series of binding models were fitted to the HMGN2-nucleosome titration data described in the text. All models assume two binding sites per nucleosome that bind HMGN2 either in an independent or cooperative manner, with some of the models including nonspecific binding of HMGN2 to DNA. Below each of the models is described in detail.

Model 1: Noncooperative Binding of HMGN2. Noting that each nucleosome is comprised of two binding sites that are assumed independent in this model, it is convenient to think about each binding event as between one such site, P, and ligand, L,

$$P + L \underset{k_{off}}{\overset{k_{on}}{\rightleftarrows}} PL, \qquad \kappa_D = [\mathrm{P}][\mathrm{L}]/[\mathrm{PL}], \qquad \textbf{[S1]}$$

where the total concentration of binding sites is twice that of the nucleosome. In Eq. **S1** κ_D is the microscopic dissociation constant and [P] and [PL] are the concentrations of unbound and ligand bound binding sites, respectively, and [L] is the concentration of free ligand. If $[\mathrm{P_T}]$ is the total nucleosome concentration in solution, then it follows that

$$2[\mathrm{P_T}] = [\mathrm{P}] + [\mathrm{PL}] \qquad \textbf{[S2]}$$

and, in a similar manner,

$$[\mathrm{L_T}] = [\mathrm{L}] + [\mathrm{PL}], \qquad \textbf{[S3]}$$

where $[\mathrm{L_T}]$ is the concentration of total ligand. An expression for [L] is readily obtained,

$$[\mathrm{L}]^2 + (2\mathrm{P_T} - \mathrm{L_T} + \kappa_D)[\mathrm{L}] - \kappa_D \mathrm{L_T} = 0 \qquad \textbf{[S4]}$$

from which the equilibrium concentration of free and bound binding sites can be derived.

The NMR and isothermal titration calorimetry (ITC) titration data described in this paper were fitted independently to this model, and to the models described below, to allow the extraction of the binding affinity and association-/dissociation-rate constants. The experimental ITC data were fitted using the procedure outlined in the manufacturer's tutorial. For the NMR titration data, we have fitted chemical shift titration profiles for several residues in the fast-to-intermediate exchange regime, as well as the observed line shape of the Val45γ2 resonance for each titration point. The NMR titration data are readily analyzed by considering the Bloch–McConnell equations (1) describing the time evolution of magnetization originating from spins in the nucleosome, $P \underset{k_{off}}{\overset{k_f}{\rightleftarrows}} PL$,

$$\frac{d\vec{M}_+}{dt} = R\vec{M}_+$$

$$\frac{d}{dt}\begin{pmatrix} M_+^P \\ M_+^{PL} \end{pmatrix} = \begin{pmatrix} i\omega_p - R_{2,P} - k_f & k_{off} \\ k_f & i\omega_{PL} - R_{2,PL} - k_{off} \end{pmatrix}\begin{pmatrix} M_+^P \\ M_+^{P} \end{pmatrix}, \qquad \textbf{[S5]}$$

where $M_+ = M_X + iM_Y$ and M_j is the j component of magnetization, ω_P and ω_{PL} are the resonance frequencies in the unbound (P) and bound (PL) states, $R_{2,P}$ and $R_{2,PL}$ are the transverse relaxation rates, and k_f is a pseudo-first-order rate constant given by $k_{on}[\mathrm{L}] = (k_{off}/\kappa_D) \cdot [\mathrm{L}]$. The time-domain signal is then calculated as

$$M_+^{total}(t) = \exp(Rt)\vec{M}_+(0), \qquad \textbf{[S6]}$$

where the initial magnetization $M_+(0)$ of the free and bound states is proportional to their fractional populations, $[\mathrm{P}]/([\mathrm{P}] + [\mathrm{PL}])$ and $[\mathrm{PL}]/([\mathrm{P}] + [\mathrm{PL}])$. Subsequently, the frequency domain profile is easily obtained after apodization and Fourier transformation, allowing the accurate extraction of chemical shift changes and line shapes. Further details of the data fitting are given below. The global fitting parameters in this model are κ and k_{off} (2). See *Details of Titration Data Fitting* below for additional details.

Model 2: Noncooperative Binding of HMGN2 Including Nonspecific DNA Binding. Before discussing this case in detail, we first consider ligand binding to a macromolecule that consists of n_1 equivalent binding sites of one type and n_2 equivalent binding sites of a second type. We further assume for the time that the two sites are independent; i.e., binding to each of the sites is not influenced by the occupancy of the other sites. Thus, each macromolecule can be "divided" into a set of n_1 molecules each with a single binding site of type 1 and a set of n_2 molecules each with a single binding site of type 2, as depicted in Scheme S1. From Scheme S1 it is clear that if the concentration of macromolecule is $[\mathrm{P_T}]$, then the concentrations of single binding molecules of types 1 and 2 are $n_1[\mathrm{P_T}]$ and $n_2[\mathrm{P_T}]$, respectively.

Consider the case of the nucleosome with $n_1 = 2$ high-affinity, specific binding sites and n_2 sites on the DNA, responsible for nonspecific binding. We can write the binding equilibria as

$$P + L \underset{k_{off}}{\overset{k_{on}}{\rightleftarrows}} PL, \qquad \kappa_D = [\mathrm{P}][\mathrm{L}]/[\mathrm{PL}] \qquad \textbf{[S7]}$$

and

$$P' + L \underset{k'_{off}}{\overset{k'_{on}}{\rightleftarrows}} PL', \qquad \kappa'_D = [\mathrm{P}'][\mathrm{L}]/[\mathrm{PL}'], \qquad \textbf{[S8]}$$

where binding of HMGN2 is to either a specific binding site (the acidic patch) [Eq. **S7**] or to an arbitrary site on the nucleosomal DNA [Eq. **S8**]. Each site (binding event) is treated independently, such that binding of the ligand to one site on the nucleosome does not preclude binding to the second site. It follows that

$$\begin{aligned} &2[\mathrm{P_T}] = [\mathrm{P}] + [\mathrm{PL}] \qquad n_2[\mathrm{P_T}] = [\mathrm{P}'] + [\mathrm{PL}'] \\ &[\mathrm{L_T}] = [\mathrm{L}] + [\mathrm{PL}] + [\mathrm{PL}']. \end{aligned} \qquad \textbf{[S9]}$$

From Eqs. **S7–S9** it can be written that

$$[\mathrm{PL}] = \frac{2[\mathrm{P_T}][\mathrm{L}]}{\kappa_D + [\mathrm{L}]}, \qquad [\mathrm{PL}'] = \frac{n_2[\mathrm{P_T}][\mathrm{L}]}{\kappa'_D + [\mathrm{L}]} \qquad \textbf{[S10]}$$

so that

$$[\mathrm{L_T}] = [\mathrm{L}] + \frac{2[\mathrm{P_T}][\mathrm{L}]}{\kappa_D + [\mathrm{L}]} + \frac{n_2[\mathrm{P_T}][\mathrm{L}]}{\kappa'_D + [\mathrm{L}]}. \qquad \textbf{[S11]}$$

An equation for [L] can be derived from the above expression,

$$[\mathrm{L}]^3 + ((2+n_2)[\mathrm{P_T}] + \kappa_D + \kappa'_D - [\mathrm{L_T}])[\mathrm{L}]^2 + (\kappa_D\kappa'_D + [\mathrm{P_T}](n_2\kappa_D + 2\kappa'_D) - [\mathrm{L_T}](\kappa_D + \kappa'_D))[\mathrm{L}] - \kappa_D\kappa'_D[\mathrm{L_T}] = 0. \quad \textbf{[S12]}$$

NMR spectra are then calculated as in Model 1, above. The global fitting parameters in this model are κ_D, k_{off}, κ'_D, and n_2. Parameters for the nonspecific DNA binding κ'_D and the stoichiometry parameter n_2 were fixed during the fitting and were estimated from the ITC data of HMGN2/nucleosomes mutants incapable of binding to the acidic patch and native gel analysis. Briefly, the observed near-constant heat effect in the ITC data recorded up to [HMGN2]/[nucleosome] = 5 indicates that at least >5 HMGN2 molecules can bind to the nucleosome in a nonspecific manner. Reasoning that this form of binding likely involves interaction of the Lys-rich area of the NBD binding to an arbitrary minor groove of the DNA, we set the stoichiometry constant n_2 to 16, corresponding to 1 HMGN2 molecule per turn. Using estimates for the microscopic affinity κ'_D of 50–200 μM, the experimental ITC curve can be reproduced. Notably, the exact value of κ'_D and n_2 do not influence the quality of the fit; they merely scale the resulting κ_D value for the specific interaction (<3-fold difference in κ_D comparing 50 and 200 μM for κ'_D with n_2 set to 16- and <2-fold difference comparing 10 and 16 for n_2 with κ'_D set to 50 uM).

Model 3. Cooperative Binding of HMGN2.

Models 1 and 2 assumed that each HMGN2 ligand binds independently to the two acidic binding pockets of the nucleosome. This condition is relaxed in the following model:

$$P + L \underset{k_{\mathrm{off},1}}{\overset{k_{\mathrm{on},1}}{\rightleftarrows}} PL_1, \qquad K_{D,1} = [\mathrm{P}][\mathrm{L}]/[\mathrm{PL_1}] = \frac{\kappa_{D1}}{2}$$
$$PL_1 + L \underset{k_{\mathrm{off},2}}{\overset{k_{\mathrm{on},2}}{\rightleftarrows}} PL_2, \qquad K_{D,2} = [\mathrm{PL_1}][\mathrm{L}]/[\mathrm{PL_2}] = 2\kappa_{D2}, \quad \textbf{[S13]}$$

where P, PL_1, and PL_2 denote unbound, singly bound, and doubly bound nucleosome, $K_{D,1}$ and $K_{D,2}$ are macroscopic dissociation constants that can be expressed in terms of the corresponding microscopic constants κ_{D1}, κ_{D2} as indicated above. When each of the sites is independent (as in model 1) $\kappa_{D1} = \kappa_{D2}$ and $K_{D,2}/K_{D,1} = 4$; alternatively when $\kappa_{D1} > \kappa_{D2}$, then $K_{D,2}/K_{D,1} < 4$ and the binding is positively cooperative. It follows that

$$[\mathrm{P_T}] = [\mathrm{P}] + [\mathrm{PL_1}] + [\mathrm{PL_2}] \qquad [\mathrm{L_T}] = [\mathrm{L}] + [\mathrm{PL_1}] + 2[\mathrm{PL_2}]. \quad \textbf{[S14]}$$

Combining Eqs. **S13** and **S14**, one can derive expressions for $[\mathrm{PL_1}]$ and $[\mathrm{PL_2}]$,

$$\left(1 - \frac{4K_{D,1}}{K_{D,2}}\right)[\mathrm{PL_1}]^3 + (K_{D,2} - 2[\mathrm{P_T}] - 4K_{D,1})[\mathrm{PL_1}]^2 + (2[\mathrm{P_T}][\mathrm{L_T}] - L_T^2 - [\mathrm{P_T}]K_{D,2} - [\mathrm{L_T}]K_{D,2} - K_{D,1}K_{D,2})[\mathrm{PL_1}] + [\mathrm{P_T}][\mathrm{L_T}]K_{D,2} = 0 \quad \textbf{[S15]}$$

and

$$[\mathrm{PL_2}] = \frac{[\mathrm{PL_1}]([\mathrm{L_T}] - [\mathrm{PL_1}])}{K_{D,2} + 2[PL_1]}. \quad \textbf{[S16]}$$

In order to fit the titration data we first consider Scheme S1. Here we have assumed that binding of a ligand to the first site does not alter the structure of the second (ligand-free) site so that the chemical shift of nuclei at the second site are unchanged. However, upon binding the second site a conformational rearrangement occurs in both sites so that $\kappa_{D1} \neq \kappa_{D2}$. Alternative schemes are, of course, possible. Based on the scheme above, we can write

$$d\vec{M}_+/dt = \begin{pmatrix} i\omega_f - R_{2,f} - 2k_{f,1} & k_{f,1} & k_{\mathrm{off},1} & 0 \\ k_{f,1} & i\omega_f - R_{2,f} - 2k_{\mathrm{off},1} - k_{f,2} & 0 & k_{\mathrm{off},2} \\ k_{f,1} & 0 & i\omega_{b,1} - R_{2,b} - k_{\mathrm{off},1} - k_{f,2} & k_{\mathrm{off},2} \\ 0 & k_{f,2} & k_{f,2} & i\omega_{b,2} - R_{2,b} - 2k_{\mathrm{off},2} \end{pmatrix}\vec{M}_+, \quad \textbf{[S17]}$$

where $\vec{M}_+ = (M_+^{P_{oo}}, M_+^{P_{01}}, M_+^{P_{10}}, M_+^{P_{11}})^+$ and "+" is transpose, $k_{f,1} = k_{\mathrm{on},1}[L] = \frac{k_{\mathrm{off},1}}{\kappa_{D,1}}[\mathrm{L}]$, $k_{f,2} = k_{\mathrm{on},2}[L]$. In addition, we assume that $k_{f,1} = k_{f,2}(k_{\mathrm{on},1} = k_{\mathrm{on},2})$, such that the change in affinity is solely due to a change in dissociation rate ($k_{\mathrm{off},2} = k_{\mathrm{off},1}\kappa_{D,2}/\kappa_{D,1}$). The initial value of the magnetization, $M_+(0)$, is given by the fractional population of each species ($[\mathrm{P}]/[\mathrm{P_T}]$, $\frac{1}{2}[\mathrm{PL_1}]/[\mathrm{P_T}]$, $\frac{1}{2}[\mathrm{PL_1}]/[\mathrm{P_T}]$, $[\mathrm{PL_2}]/[\mathrm{P_T}]$). As described above, spectra are calculated by first solving Eq. **S17** to obtain the time evolution of magnetization, followed by Fourier transformation of the free induction decay (FID_. The global fitting parameters in this model are $\kappa_{D,1}$, $\kappa_{D,2}$, and $k_{\mathrm{off},1}$ (three parameters; $k_{\mathrm{off},2}$ is fixed using the formula given above). See *Details of Titration Data Fitting* below for additional details.

Model 4. Cooperative Binding of HMGN2 Including Nonspecific DNA Binding.

Here we consider a combination of Models 2 and 3 with the assumption that specific and nonspecific binding are independent events:

$$P + L \underset{k_{\mathrm{off},1}}{\overset{k_{\mathrm{on},1}}{\rightleftarrows}} PL_1, \qquad K_{D,1} = [\mathrm{P}][\mathrm{L}]/[\mathrm{PL_1}] = \frac{\kappa_{D1}}{2}$$
$$PL_1 + L \underset{k_{\mathrm{off},2}}{\overset{k_{\mathrm{on},2}}{\rightleftarrows}} PL_2, \qquad K_{D,2} = [\mathrm{PL_1}][\mathrm{L}]/[\mathrm{PL_2}] = 2\kappa_{D2} \quad \textbf{[S18]}$$
$$P' + L \underset{k'_{\mathrm{off}}}{\overset{k'_{\mathrm{on}}}{\rightleftarrows}} PL', \qquad \kappa' = [\mathrm{P}'][\mathrm{L}]/[\mathrm{PL}'].$$

Following what has already been described,

$$[\mathrm{P_T}] = [\mathrm{P}] + [\mathrm{PL_1}] + [\mathrm{PL_2}] \qquad n_2[\mathrm{P_T}] = [\mathrm{P}'] + [\mathrm{PL}']$$
$$[\mathrm{L_T}] = [\mathrm{L}] + [\mathrm{PL_1}] + 2[\mathrm{PL_2}] + [\mathrm{PL}']. \quad \textbf{[S19]}$$

Eqs. **S18** and **S19** can be combined to generate the following expressions:

$$[\mathrm{P}] = \frac{[\mathrm{P_T}]K_{D,1}K_{D,2}}{K_{D,1}K_{D,2} + K_{D,2}[\mathrm{L}] + [\mathrm{L}]^2}, \qquad f_P = \frac{[\mathrm{P}]}{[\mathrm{P_T}]}$$
$$[\mathrm{PL_1}] = \frac{[\mathrm{P_T}]K_{D,2}[\mathrm{L}]}{K_{D,1}K_{D,2} + K_{D,2}[\mathrm{L}] + [\mathrm{L}]^2}, \qquad f_{PL1} = \frac{[\mathrm{PL_1}]}{[\mathrm{P_T}]}$$
$$[\mathrm{PL_2}] = \frac{[\mathrm{P_T}][\mathrm{L}]^2}{K_{D,1}K_{D,2} + K_{D,2}[\mathrm{L}] + [\mathrm{L}]^2}, \qquad f_{PL2} = \frac{[\mathrm{PL_2}]}{[\mathrm{P_T}]}$$
$$[\mathrm{PL}'] = \frac{n_2[\mathrm{P_T}][\mathrm{L}]}{\kappa'_D + [\mathrm{L}]}, \qquad f_{PL'} = \frac{[\mathrm{L}]}{\kappa'_D + [\mathrm{L}]} \quad \textbf{[S20]}$$

that are then combined with the last relation in Eq. **S19** to yield

$$[L]^4 + (K_{D,2} + \kappa'_D + (2+n_2)[P_T] - [L_T])[L]^3 + (K_{D,1}K_{D,2} + K_{D,2}\kappa'_D + (1+n_2)[P_T]K_{D,2} + 2[P_T]\kappa'_D) - [L_T](K_{D,2} + \kappa'_D))[L]^2 + (K_{D,1}K_{D,2}\kappa'_D + [P_T]K_{D,2}\kappa'_D + n_2[P_T]K_{D,1}K_{D,2} - [L_T](K_{D,1}K_{D,2} + K_{D,2}\kappa'_D))[L] - [L_T]K_{D,1}K_{D,2}\kappa'_D = 0. \quad \textbf{[S21]}$$

Spectra can be simulated exactly as per Model 3 using the f_j values defined in Eq. **S20**. The global fitting parameters in this model are $\kappa_{D,1}$, $\kappa_{D,2}$, $k_{off,1}$, κ'_D, and n_2 (five parameters; $k_{off,2}$ is fixed according to $k_{off,2} = k_{off,1}\kappa_{D,2}/\kappa_{D,1}$ and the parameters for nonspecific binding are set as for Model 2).

Details of Titration Data Fitting.

In order to determine the binding affinities and association/dissociation rates of the HMGN2-nucleosome interaction, we fitted simultaneously chemical shift titration curves, and line shapes obtained from the titration of H2B-labeled nucleosomes to the binding models described above. We now describe the simulation and fitting procedure for each of these three types of data in some detail.

i. Chemical shift titration curves were included for all resonances for which either in the ^{1}H or ^{13}C dimension a significant change was noted (>5 Hz) and for which only a single peak was observed during titration; i.e., the exchange regime is either fast or fast-to-intermediate. The maximum chemical shift change for these selected resonances was approximately 17 Hz; i.e., $\Delta\omega = \sim 110$ s^{-1}. Resonances that were overlapping with other peaks were excluded, as were resonances that were in the intermediate exchange regime in the orthogonal dimension. The final set consisted of seven binding curves. For six of these, no line broadening was observed during the titration as determined from a comparison of peak intensities between initial and final spectrum. For these residues the difference in transverse relaxation rates ΔR_2 was set to zero. For one residue corresponding to L103δ1 of H2B, line width estimation indicated an approximately 1.5-fold increase of R_2 and ΔR_2 was set accordingly. The R_2 in the free state was set to 50 s^{-1} for both ^{13}C and ^{1}H, based on relaxation measurements. The chemical shifts of the free and the bound state were fixed to the observed peak positions in the initial and the final spectrum. The titration curves were derived from peak positions in the simulated spectra. Spectra were reconstructed as a sum of Lorentzians with frequencies and line widths given by the imaginary and real components of the eigenvalues of the exchange matrix (as given in Eq. **S5** or **S17**) and intensity and phase derived from its eigenvectors and the equilibrium populations. In fits using the cooperative binding models, the chemical shift of the singly bound state, $\omega_{b,1}$ was fixed to the chemical shift of the fully bound state, $\omega_{b,2}$ for all residues except one. To also account for the experimental error in the initial peak position, and thus a nonzero initial value, a (small) constant offset term was added to the simulated chemical shift difference so as to minimize the differences between the simulated and experimental values. The χ^2 and the degrees of freedom (DOF) were calculated as

$$\chi^2_{CS} = \sum_j^M \sum_i^N \left(\frac{\delta_{calc}(\kappa_D, k_{off}, \text{offset}) - \delta_{obs}}{\sigma_{nucleus}} \right)$$

$$\text{DOF}_{CS} = NM - M - 3 - \theta_m - \varphi_m,$$

where δ is the peak position, nucleus = ^{13}C or ^{1}H, σ_{1H} = 0.6 Hz and σ_{13C} = 1.0 Hz, i runs over all N (=17) titration points and j runs over all M selected resonances (=7). The degrees of freedom are equal to total number of points NM compensated for the M offset variables, one ΔR_2 value used to fit the curve in the fast-to-intermediate exchange regime, the number of global variables θ_m for each model (m = 1–4; $\theta_1 = 2$, $\theta_2 = 4$, $\theta_3 = 3$, $\theta_4 = 5$) and one chemical shift of the singly bound state in the cooperative model ($\varphi_{1/2} = 0$ and $\varphi_{3/4} = 1$).

ii. Fitting the line shape of Val45γ2 in the ^{13}C dimension during the titration. This resonance does not overlap and shows a large chemical shift change predominantly in the ^{13}C dimension. It is in the slow-to-intermediate exchange time scale allowing estimation of k_{off}. The relaxation rates and chemical shifts of the free and bound states were derived from the initial and final spectrum. In case of the cooperative binding models, the chemical shift of the singly bound state, $\omega_{b,1}$, was a fitting variable. The simulated FID was transformed using the experimental processing scheme. Each simulated spectrum was scaled to match the observed maximum intensity to compensate for relaxation losses during the transfer delays and the effect of exchange in the orthogonal dimension. The χ^2 and the DOF were calculated as

$$\chi^2_{LS} = \sum_i^N \sum_k^Q \left(\frac{I_{calc}(\kappa_D, k_{off}, \text{scaling}_{factor}) - I_{obs}}{\sigma_k} \right)^2$$

$$\text{DOF}_{LS} = NQ - N - 2 - \theta_m - \varphi_m,$$

where I is the intensity, σ_k is set to the noise level of each spectrum, i runs over all N titration points, and j runs over all Q data points in the spectrum. The degrees of freedom are equal to total number of points NQ compensated for the N scaling variables, the R_2 for the free and bound state, the number of global variables θ_m for each model (m = 1–4; $\theta_1 = 2$, $\theta_2 = 4$, $\theta_3 = 3$, $\theta_4 = 5$), and the chemical shift of the singly bound state in the cooperative model ($\varphi_{1/2} = 0$ and $\varphi_{3/4} = 1$).

The procedures outlined above were implemented in MatLAB scripts (MATLAB version 7.6.0. The MathWorks Inc.). Minimization of the fitting parameters was carried out using the "fminsearch" function that uses the unconstrained nonlinear Nelder–Mead minimization algorithm. A global χ^2 was defined as

$$\chi^2_{global} = \frac{\chi^2_{CS}}{\text{DOF}_{CS}} + \frac{\chi^2_{LS}}{\text{DOF}_{LS}} \qquad \chi^2_{global,ave} = \chi^2_{global}/2.$$

The weighting factors of the individual χ^2-values were set to the degrees of freedom of each measurement type so that they contribute equally to the global χ^2. Individual fits of each measurement showed that (at least for Model 1) each dataset minimized to very similar values with similar reduced χ^2-values, indicating that each measurement can be weighed equally. An overview of the fitting results for all models is given in Fig. S6.

In fitting the ITC data χ^2 was defined as

$$\chi^2_{ITC} = \sum_k^S \left(\frac{H_{calc}(\kappa_D, n) - H_{obs}}{\sigma} \right)^2 \qquad \text{DOF}_{ITC} = S - \varphi_m$$

$$\chi^2_{ITC,red} = \chi^2_{ITC}/\text{DOF}_{ITC},$$

where σ is set based on duplicate measurements and k runs over all S points in the ITC curve. The degrees of freedom are equal to the total number of points S compensated for the number of fitting parameters φ_m(m = 1–4; $\varphi_1 = 2(\kappa_D, \Delta H)$, $\varphi_2 = 5(\kappa_D, \Delta H, \kappa', n_2, \Delta H')$, $\varphi_3 = 4(\kappa_{D,1}, \Delta H_1, \kappa_{D,2}, \Delta H_2)$, $\varphi_4 = 7(\kappa_{D,1},$

$\Delta H_1, \kappa_{D,2}, \Delta H_2, \kappa', n_2, \Delta H'$). The ITC data alone do not allow discrimination of cooperative or noncooperative binding; i.e., it is equally well fitted using model 2 or model 4. However, the NMR data are best fit using a cooperative model (model 4), consistent with previous observations that binding becomes cooperative above 20–30 mM ionic strength (2). Excellent fits of the ITC data are obtained assuming a cooperative model (Fig. 3*A*). To extract relative affinities of mutant nucleosomes or mutant HMGN2, all ITC data were fitted to model 2 (Table S2).

Modeling of the HMGN2-Nucleosome Complex. We used the experimental mutagenesis, paramagnetic relaxation enhancement (PRE), and titration data described in the text to create a structural model for the HMGN2-nucleosome complex. Guided by the experimental data, we docked the nucleosome binding domain (NBD) of HMGN2 to the nucleosome using HADDOCK version 2.1 (3), installed on the National Institutes of Health Biowulf server. In what follows, we describe the docking procedure.

As a first step, we reduced the complexity of the system by considering only a binary complex between residues 21–28 of HMGN2, corresponding to the N-terminal part of the NBD, and a histone hemioctamer (H2A-H2B-H3-H3-H4). NMR experiments showed that the $HMGN2_{21–28}$ region binds to the acidic patch of the isolated H2A-H2B dimer (Fig. S6), which is further supported by our ITC mutagenesis data (Fig. 3*A*). The initial conformation of the $HMGN2_{21–28}$ fragment was built using PyMol (4), and the octamer structure was taken from the nucleosome crystal structure (PDB ID code 2PYO). Four residues in $HMGN2_{21–28}$, Arg22, Ser24, Arg26, and Leu27, were selected as active residues, based on our results and previous mutational studies (5). On the side of the histones, residues Asp60, Glu63, Asp89, Glu90, and Glu91 in H2A and Glu102 in H2B were selected as active residues based on the mutagenesis data. In addition, Leu64 in H2A and Val45 and Leu103 in H2B were included on the basis of the observed chemical shift perturbations. Finally, as a potential hydrogen bond donor/acceptor, His106 in H2B was also selected as an active residue. No passive residues were defined. Ambiguous interaction restraints (AIRs) were defined between the active residues in the HMGN2 fragment and the active residues in histones H2A/H2B.

These restraints were subsequently used to dock the HMGN2 fragment onto the histone H2A-H2B surface, following the standard HADDOCK protocols, with the modification that (*i*) the $HMGN2_{21–28}$ fragment was allowed to move freely during the simulated annealing phase and (*ii*) the $HMGN2_{21–28}$ fragment was placed close to histones H2A and H2B manually. Briefly, a total of 1,000 docking solutions were generated during the rigid-body energy minimization step (it0) and were subsequently subjected to simulated annealing (it1) during which the backbone and side chain atoms of the $HMGN2_{21–28}$ were free to move. The resulting structures were sorted according to intermolecular energy (sum of the van der Waals, electrostatic, and AIRs energy), and the best 200 structures were clustered using a 7.5-Å backbone rmsd cutoff and a minimum of four structures per cluster. In most of the clusters, the side chain of Arg26 in HMGN2 converges to a similar conformation with its guanidinium group interacting with the side chains of Glu63, Asp89, and Glu91 of H2A and Glu102 of H2B in the acidic patch, whereas other residues in HMGN2 did not show obvious convergence.

Next, we considered the ternary system formed by HMGN2, histones, and DNA. We used an extended fragment of HMGN2, residues 18–44, thus including its DNA interaction region (see Fig. 2) and built its initial conformation using PyMol. Rather than confining the HMGN2-DNA interaction to Lys35, Lys39, and Lys41 as identified by mutagenesis, ambiguous interaction restraints were defined between residues 28–43 in $HMGN2_{18–44}$ and the DNA region near the entry/exit point. In a conservative approach, the αN-helix of H3, which is close to this part of the DNA, was also included as a potential interaction site (see Fig. S6). The interaction with the acidic patch was modeled in two parts: (*i*) to allow a broad range of conformations in the complex, comprehensive AIRs were defined between residues 19–35 of $HMGN2_{18–44}$ and all exposed residues of H2A and H2B, except the C-terminal 14 residues of H2A (Fig. S6); (*ii*) to anchor $HMGN2_{18–44}$ on the acidic patch, unambiguous distances restraints between the guanidinium group carbon atom of Arg26 and the side chain atoms of Glu63, Asp89, and Glu91 in H2A and Glu102 in H2B were derived from the docking solutions in the first step. No passive residues were chosen.

A three-body docking protocol was followed with identical parameters as in the first step, with the modification that the starting conformations were not randomized to ensure that the histone-DNA interaction was not disrupted. $HMGN2_{18–44}$ was manually put on top of the nucleosome structure with the N-terminal region close to the acidic patch in H2A and H2B and the C-terminal region close to the DNA near the entry/exit point and subjected to rigid-body minimization followed by simulated annealing. The 200 docking solutions with lowest energies were clustered with a backbone rmsd cutoff of 5.0 Å and a minimum of 15 structures per cluster. The largest cluster, with 20 structures, was chosen for further refinement. One structure from this cluster was selected as the starting conformation for a subsequent, identical docking calculation to refine the local structure. This procedure was repeated one more time. The 200 lowest energy structures from the final calculation were clustered using a backbone rmsd cutoff of 3 Å. The largest cluster, with 13 structures, was selected as the structure model for the HMGN2-nucleosome complex. A representative structure from this cluster is shown in Fig. S6). For backbone dihedral angles in this selected cluster, 28.8% of them are in the most favored region, 48.7% are in the additional allowed region, 13.3% are in generally allowed region, and 9.3% are in the disallowed region. No effort to improve the quality of the structure (such as refinement with explicit water) is made because the major conclusion in the manuscript is independent of the details of the structures.

1. McConnell HM (1958) Reaction rates by nuclear magnetic resonance. *J Phys Chem* 28:430–431.
2. Schroter H, Bode J (1982) The binding sites for large and small high-mobility-group (HMG) proteins. Studies on HMG-nucleosome interactions in vitro. *Eur J Biochem* 127:429–436.
3. Dominguez C, Boelens R, Bonvin AMJJ (2003) HADDOCK: A protein-protein docking approach based on biochemical or biophysical information. *J Am Chem Soc* 125:1731–1737.
4. DeLano WL (2002) The PyMOL molecular graphics system (DeLano Scientific, San Carlos, CA).
5. Ueda T, Catez F, Gerlitz G, Bustin M (2008) Delineation of the protein module that anchors HMGN proteins to nucleosomes in the chromatin of living cells. *Mol Cell Biol* 28:2872–2883.

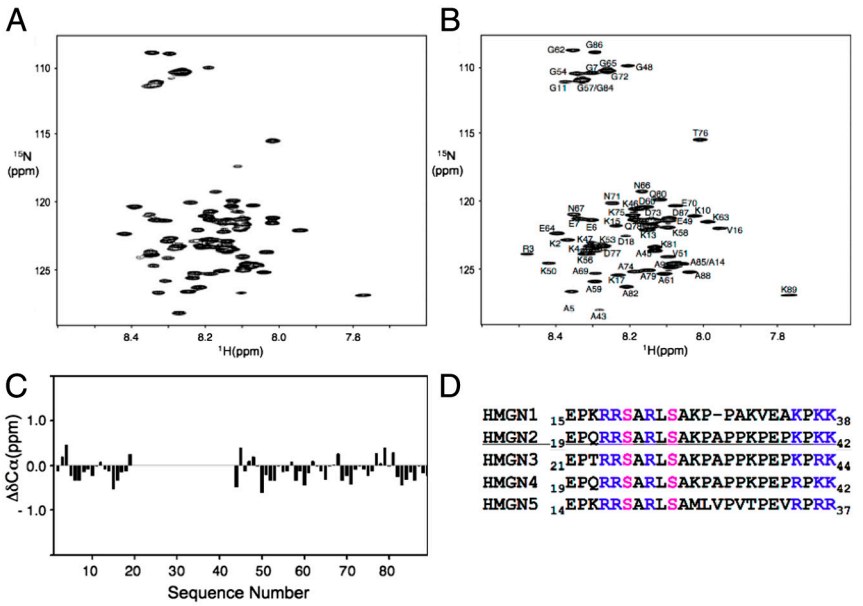

Fig. S1. *HMGN2 is intrinsically disordered and binds to the nucleosome with its nucleosome binding domain (NBD, residues 19–42).* (*A*) ^{1}H-^{15}N transverse relaxation optimized nuclear magnetic resonance spectroscopy (TROSY) spectrum of free HMGN2. The limited dispersion of amide cross-peaks (approximately 7.9–8.5 ppm in ^{1}H dimension) is consistent with its intrinsically disordered nature. (*B*) ^{1}H-^{15}N TROSY spectrum of HMGN2 bound to the nucleosome. Residues in the disordered N- and C-terminal tails of HMGN2 give rise to sharp resonances, whereas residues 19 to 42 (the NBD) are not observed. This indicates that only the NBD binds to the nucleosome, whereas the terminal tails remain very flexible in the HMGN2-nucleosome complex. HMGN2 was assigned using standard solution NMR methods. Note that some of the peaks in the flexible region of HMGN2 in the HMGN2-nucleosome complex have different chemical shifts when compared with those in the free HMGN2, indicating that there are transient interactions between the flexible region of HMGN2 and the nucleoosme. (*C*) The deviation of Cα chemical shifts from random coil values for the tails in the HMGN2-nucleosome complex is well within ±1 ppm, consistent with a disordered conformation in the bound state. (*D*) Sequence alignment of the NBD in the different human HMGNs, showing the absolute conservation of the R-S-RL motif and the conservation of a Lys- (Arg)-rich region in the C-terminal part of the NBD. Color coding: blue, Arg/Lys; magenta, Ser24 and Ser28. HMGN2 is underlined.

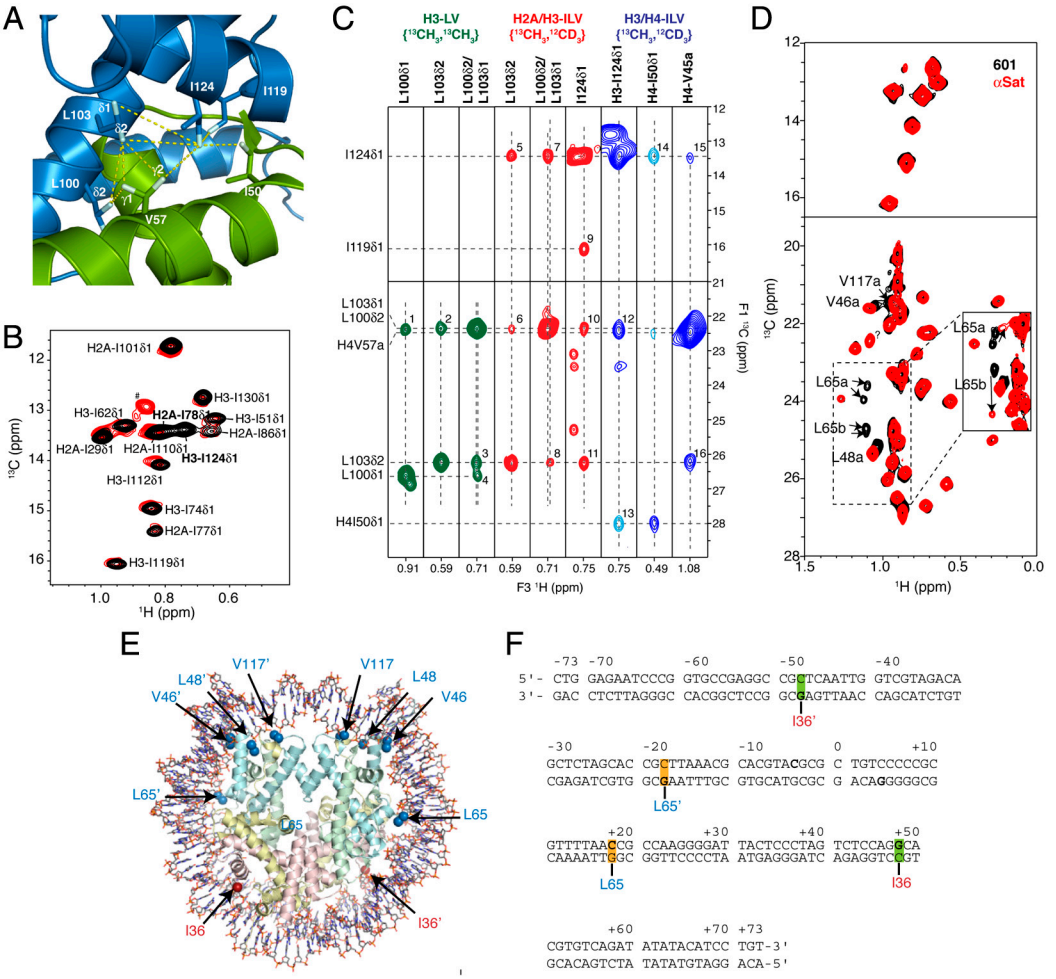

Fig. S2. *Example of assignment strategy by mutations and structure-based NOESY analysis and effect of asymmetrical DNA sequence on methyl chemical shifts in the nucleosome*. (*A*) Part of the crystal structure of the nucleosome (Protein Data Bank ID code 2PYO), focusing on the methyl groups surrounding H3-Ile124δ1. Observed NOEs are indicated by dashed yellow lines. (*B*) Assignment of H3-Ile124 by site-directed mutagenesis. Overlay of methyl-TROSY spectra of wild-type nucleosome with Ile, Leu, and Val (ILV)-labeled H2A and H3 (black) and H2A-Ile78Val/H3-Ile124Val double-mutant nucleosome (red). The double-mutant spectrum lacks two cross-peaks, which must therefore correspond to H2A-Ile78δ1 and H3-Ile124δ1. Of these two, the peak at 13.4 ppm/0.75 ppm (^{13}C, ^{1}H) originates from H3, allowing its unambiguous assignment to H3-Ile124δ1. The peak marked with a # is an artifact. (*C*) Assignment of a cluster of methyl groups surrounding H3-Ile124 by NOEs. Selected strips from 3D heteronuclear multiple quantum coherence (HMQC)-NOESY-HMQC spectra of nucleosomes are shown; the labeling scheme used for each spectrum is indicated (*Top*). Starting from the assignment of H3-Ile124δ1, cross-peaks 9 and 11 in the H2A/H3 ILV-labeled NOESY (shown in red) can be immediately assigned to I119δ1 and one of the methyl groups of L103, because these are the only close methyl groups in H3. Ile and Leu residues can be easily distinguished based on their chemical shifts. The corresponding strips of L103 show the reciprocal NOE to Ile124 (cross-peak 5; the strip from I119 is not shown). Using the NOESY recorded on a sample in which both methyl groups in Leu/Val residues are labeled (shown in green), we can identify the resonance belonging to the second methyl group of L103 resonances using cross-peaks 2 and 3. The additional cross-peak in the strip of L103δ2 indicates that there are two overlapping spin systems. Cross-peak 6 in the regular NOESY shows that L103δ2 is spatially close to this overlapping resonance, suggesting that this is a methyl group of L100. Only the δ2 methyl groups of L100 and L103 are close enough to give rise to a NOE cross-peak, allowing their stereospecific assignment and assignment of the reciprocal cross-peak 8. Note that this stereospecific assignment was confirmed by low crystallographic B factors and high S^2 order parameters for these residues, indicating that the side chains have a rigid orientation in the crystal and as well as in solution. Furthermore, their chemical shift difference $\Delta\delta = \delta^{\delta 1} - \delta^{\delta 2}$ corresponds with the observed χ_2-angle in the crystal structure (+4.6 ppm/trans for L100; −3.8 ppm/gauche+ for L103) (1). Using an H3/H4 ILV-labeled sample (shown in blue), we can extend these assignments over the H3/H4 interface. The folded cross-peak 13 originates from an Ile in H4, which must be Ile50δ1 of H4. Note that the diagonal peak in the strip of H4-Ile50δ1 is very weak, but the reciprocal NOE is clearly visible (cross-peak 14). In addition, H3-Ile124 is close to a Leu/Val methyl group of H4 as indicated by cross-peaks 12 and 15, which must be a methyl group of V57. This is further confirmed by a NOE between from that methyl group in V57 to L103δ2, cross-peak 16. List of NOE cross-peak assignments: 1 (L100δ1-L100δ2); 2 (L103δ2-L103δ1); 3 (L103δ1-L103δ2); 4 (L100δ2-L100δ1); 5 (L103δ2-I124δ1); 6 (L103δ2-L100δ2); 7 (L103δ2-I124δ1); 8 (L100δ2-L103δ2); 9 (I124δ1-I119δ1); 10 (I124δ1-L103δ1); 11 (I124δ1-L103δ2); 12 (H3-Ile124δ1-H3-L103δ1) and (H3-Ile124δ1-H4-V57a); 13 (H3-Ile124δ1-H4-I50δ1); 14 (H4-I50δ1–H3-Ile124δ1); 15 (H4-V57a–H3-Ile124δ1); 16 (H4-V57a-H3-L103δ2). (*D*) Overlay of the methyl-TROSY spectra of nucleosomes reconstituted with ILV-labeled H3 and nonsymmetrical "601" (black) and symmetrical human α-satellite (red) DNA. (*Top*) The δ1 methyl groups of Ile residues. (*Bottom*) The Leu-δ1/δ2 and Val-γ1/γ2 methyl-groups. Methyl groups that are close to the DNA (see *E*) show significant chemical shift changes and are labeled. The methyl groups of L65 give rise to split cross-peaks in 601-nucleosomes as they are close to an asymmetric site in the 601-DNA sequence (see below). In the symmetrical α-satellite nucleosomes, L65 methyl resonance is singular but very weak (see *Inset*), as they are very close (3.1 Å shortest ^{1}H-^{1}H distance) to the 5-methyl group of thymidine (2), causing efficient relaxation. No such proximity occurs to other methyl groups. The cross-peak marked with ? likely corresponds to a methyl group of either V46 or V117. (*E*) Cartoon representation of the nucleosome structure showing the H3 methyl groups that are close to the DNA as spheres. The location of I36 in H2B, which is also close to the DNA, is also indicated. Color coding: H2A, orange; H2B, red; H3, blue; H4, green; DNA, gray. (*F*) Sequence of the 601 DNA, the base pair at the dyad axis is position 0. The location of L65 in H3 is indicated; the closest base is emphasized in bold. In the 601-nucleosome structure (3), L65 methyl groups are closest to the H5 atom of a cytosine base at position +18 (3.3 Å), whereas at the symmetry related position −18 the methyls of L65′ are closest to the H8 of thymidine (3.5 Å). Interestingly, the I36δ1 methyl group in H2B is 4.0 Å from the H8 of guanidine at both position +48 and −48. Corresponding with the

local symmetry in the sequence, the I36δ1 cross-peak is singular. Residues V46, L48, and V117 in H3 are close to the DNA, but are more than 6 Å away from any atom in the bases such that their resonances will be less sensitive to the local asymmetry of the DNA.

1. Mulder FAA (2009) Leucine side-chain conformation and dynamics in proteins from 13C NMR chemcial shifts. *Chembiochem* 10:1477–1479.
2. Clapier CR, et al. (2008) Structure of the Drosophila nucleosome core particle highlights evolutionary constraints on the H2A-H2B histone dimer. *Proteins* 71:1–7.
3. Makde RD, England JR, Yennawar HP, Tan S (2010) Structure of RCC1 chromatin factor bound to the nucleosome core particle. *Nature* 467:562–566.

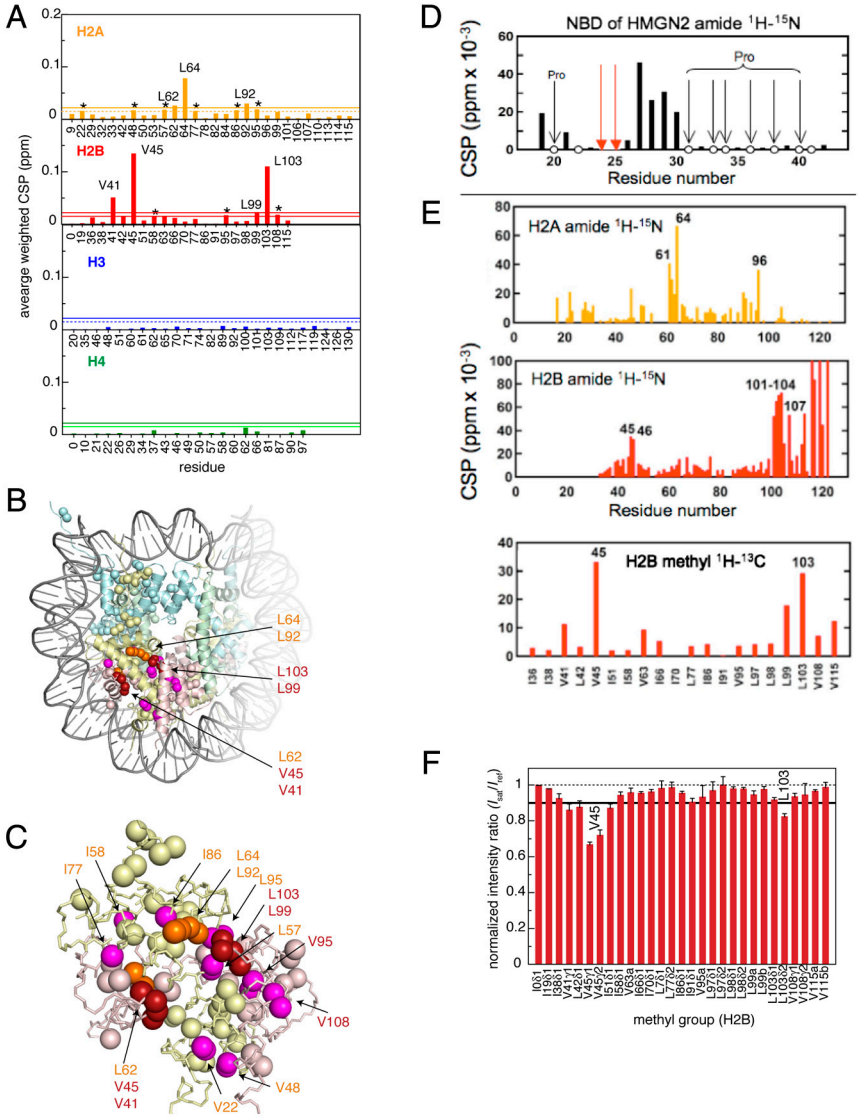

Fig. S3. *Chemical shift perturbation upon HMGN2 binding identifies the acidic patch as the binding surface*. (*A*) Chemical shift perturbation (CSP) between free and HMGN2 bound nucleosome for all ILV residues in H2A, H2B, H3, and H4. Residues with averaged, weighted CSP larger than the 10% trimmed mean + 2 SD are labeled. Note that this threshold (0.022 ppm; solid line) was calculated using the H2A and H2B datasets only. Using all four datasets, the threshold becomes 0.015 ppm (broken line). The residues additionally identified as significant using the latter criterion are indicated with *. (*B*) Structure of the nucleosome showing all ILV methyl groups with spheres. Residues with significant chemical shift changes (shown labeled in *A*) are labeled and color coded: orange, H2A; red, H2B. Residues with chemical shift perturbation larger than 0.015 ppm are shown in magenta. (*C*) Detail of the H2A-H2B dimer structure, showing all ILV methyl groups with spheres. Color coding as in *B*. The additionally identified residues are either directly neighboring the residues with largest chemical shift changes or are part of the groove between the α2-helix in H2A and the αC-helix in H2B. The observed changes for residue I58 in H2A, which is buried, might suggest subtle structural rearrangements in the H2A-H2B dimer upon HMGN2 binding. (*D*) Chemical shift perturbation experiments show that the N-terminal region of the NBD interacts weakly with the acidic patch of the isolated H2A-H2B dimer. Amide ^{1}H-^{15}N CSP of the NBD region of HMGN2 due to binding of H2A-H2B dimer. Red arrows indicate that the peaks for residues 24 and 25 disappeared upon adding H2A-H2B to HMGN2. Open circles indicate either unassigned peaks or Pro residues. H2A-H2B dimer is present in approximately 10-fold molar excess over HMGN2. (*E*) Observed chemical shift changes between wild-type H2A-H2B dimer and a fusion H2A-H2B dimer, where the HMGN2-NBD is covalently linked to H2B ($H2B_{27–122}$-GGGGGGGG-$HMGN2_{16–35}$). Chemical shift changes are reported for the amide ^{1}H-^{15}N in H2A (*Top*), H2B (*Middle*), and the methyl ^{1}H-^{13}C in H2B (*Bottom*) and were calculated using $\Delta(\delta^{1}\mathrm{H}\text{-}^{15}\mathrm{N}) = [(\Delta\delta^{1}\mathrm{H})^2 + (\Delta\delta^{15}\mathrm{N}/5)^2]^{1/2}$ and $\Delta(\delta^{1}\mathrm{H}\text{-}^{13}\mathrm{C}) = [(\Delta\delta^{1}\mathrm{H})^2 + (\Delta\delta^{13}\mathrm{C}/4)^2]^{1/2}$, respectively. (*F*) Saturation transfer experiment confirms close proximity between H2B V45/L103 and HMGN2. Normalized ratios of peak intensities in methyl-TROSY spectra of nucleosomes with ILV-labeled H2B either acquired after saturation of HMGN2 protons, I_{sat}, or without their saturation, I_{ref}. In the saturation experiment, aliphatic HMGN2 protons (3.2 ± 1 ppm) were saturated, whereas in the reference experiment, the carrier was placed at −1.8 ppm during saturation. The peak intensity ratio I_{sat}/I_{ref} was normalized with respect to the I_{sat}/I_{ref} ratio obtained for free nucleosomes using identical experimental settings. Errors (1 SD) are denoted by thin bars. Methyl groups with normalized intensity ratio + 2 SD < 0.9 were considered significant. Measurements were done at 35 °C at a nucleosome:HMGN2 molar ratio of 1:1.5 to avoid effects from nonspecific binding. To ensure fast exchange between free and bound forms, measurements were done at pD 6.0, where the exchange rate is approximately 1,000–1,500 s^{-1}.

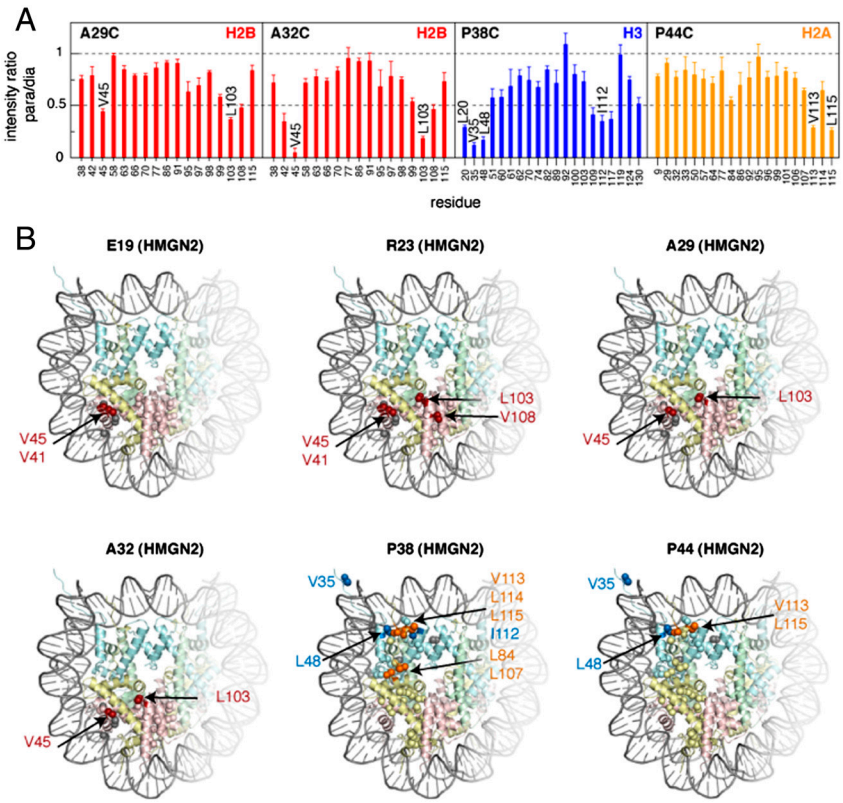

Fig. S4. *Paramagnetic spin-labeling experiments identify two interaction sites for the NBD*. (*A*) Methyl group peak intensity ratios, $I(Mn^{2+})/I(Ca^{2+})$, of paramagnetic Mn^{2+}-EDTA and diamagnetic Ca^{2+}-EDTA spin-labeled HMGN2 at positions 29, 32, 38, and 44. Intensity ratios of the two individual methyl groups for Leu/Val were averaged. Errors (1 SD) are denoted by thin bars. Residues with average intensity ratio + 2 SD < 0.5 are labeled. (*B*) Structural summary of paramagnetic spin-labeling experiments. Methyl groups with large decreases in peak intensity are highlighted and labeled for each spin-labeled HMGN2 mutant. Methyl groups without significant attenuation are shown in light colors. Methyl groups for which no PRE data are available, either due to overlap or weak peak intensities in the diamagnetic state, are shown in gray. Spin labels in the N-terminal part of the NBD (E19, R23, A29, and A23) affect the acidic patch region on the H2A-H2B dimer, whereas spin labels in the C-terminal part of the NBD affect the methyl groups in the H2A C-terminal region and H3 N-terminal region. Color coding: methyl groups in H2A, H2B, and H3 are shown in light orange, light red, and light blue, respectively.

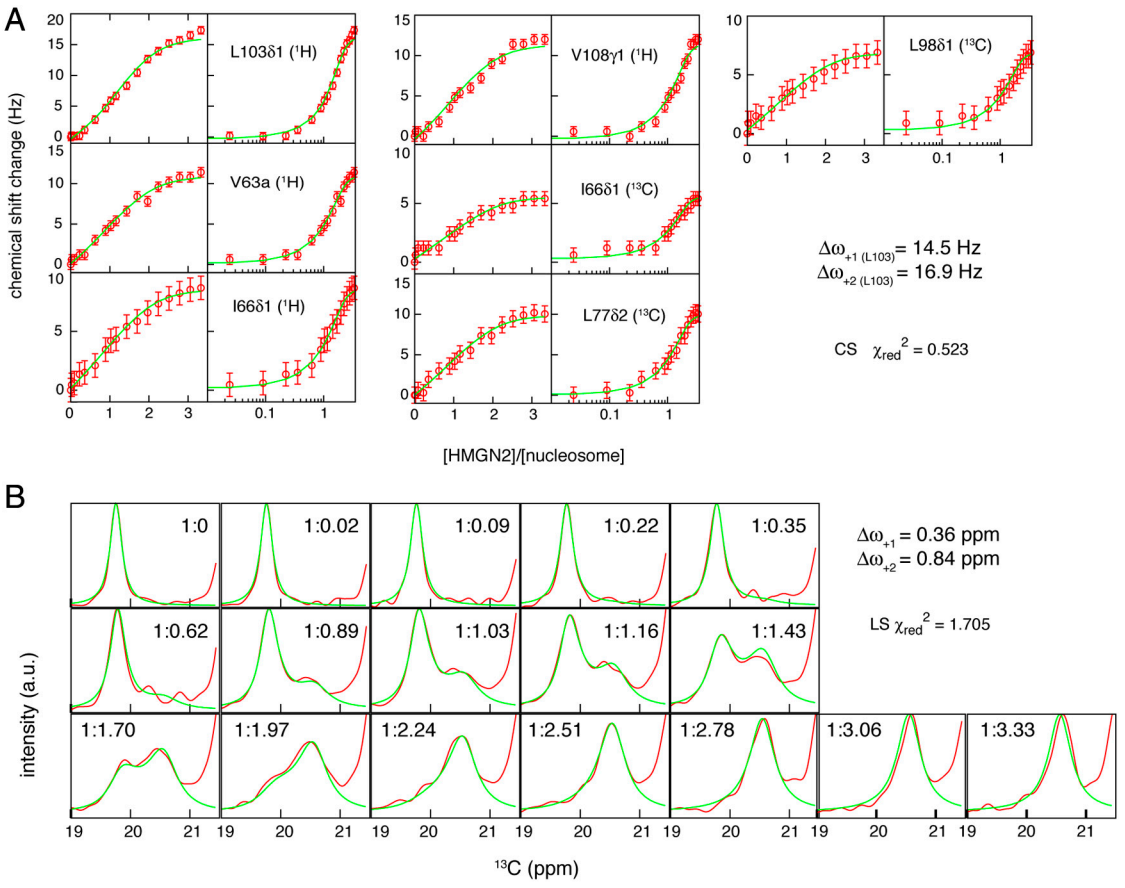

C

model	κ / $\kappa_{D,1}$ (μM)	$\kappa_{D,2}$ (μM)	$k_{off,1}$ (s^{-1})	$k_{off,2}$ (s^{-1})	n_H	κ (μM, fixed)	n_2 (fixed)	global χ^2_{red}	CS χ^2_{red}	LS χ^2_{red}	ITC χ^2_{red}
1	28.6	-	83.2	-	-	-	-	3.27	1.17	5.36	(1327)
2	0.71	-	87.6	-	-	50	16	2.89	1.05	4.73	(39)
3	19.2	6.84	142	50.7	1.25	-	-	1.41	0.77	2.06	(270)
4	1.40	0.17	425	50.8	1.48	50	16	1.11	0.52	1.71	(24)

Fig. S5. *Fits of NMR titration data to cooperative binding model including weak, nonspecific DNA binding.* (*A*) Experimental (red) and simulated (green) chemical shift perturbation curves for all residues that were included in the fit in linear and semilog plots. The final reduced χ^2 of the fit is indicated as well as the fitted value for $\Delta\omega_{+1}$ (the shift difference between the free and singly bound state) for L103δ1. The fixed value for $\Delta\omega_{+2}$ is shown as a reference. (*B*) Experimental (red) and simulated (green) line shapes of V45γ2 during the titration. Ratios of nucleosome:HMGN2 are indicated in the top of each spectrum trace. The final reduced χ^2 of the fit is indicated as well as the fitted value for $\Delta\omega_{+1}$. The fixed value for $\Delta\omega_{+2}$ is shown as a reference. Best-fit parameters indicate that the HMGN2-nucleosome interaction is tight (K_D is 0.17 μM for the second ligand and effective overall K_D is approximately 0.5 μM), yet highly dynamic. The on rate of complex formation (approximately $3 \cdot 10^8$ M^{-1} s^{-1}) is higher than expected for pure diffusion controlled reaction due to favorable electrostatic interactions. The lifetime of the fully bound state is approximately 20 ms, providing an upper limit for the lifetime at higher ionic strength. Correspondingly, in vivo fluorescence measurements have shown that HMGN2 is highly mobile in the nucleus, traveling over a micrometer in approximately 2 s (1, 2). Combined with the high association and dissociation rates for binding to a single nucleosome as derived from the NMR data, this suggests that HMGN2 could bind chromatin in a "hopping" mode, in which it reassociates quickly with a nearby nucleosome after dissociating such that its overall diffusion is much slower effectively. Such a mechanism was also proposed for another chromatin binding transcription factor where electrostatics play a prominent role in binding and with a similar effective in vivo diffusion constant as HMGN2 (3). In fact, based on a detailed fluorescence study, it was concluded that the upper limit for lifetime of the chromatin bound state was approximately 25 ms, in excellent correspondence with our estimates for HMGN2. (*C*) Comparison of quality of fit of NMR data to several binding models. The Hill coefficient, n_H, was calculated as the maximum slope of the derivative of the binding curve using best-fit parameters; ITC data were not used in the fit; reported reduced χ^2 is based on simulation using the best-fit parameters. Model 4 gives the lowest overall reduced χ^2. The line shapes fits are statistically better fit using model 4 at the 5% significance level as shown by F test.

1. Phair RD, Misteli T (2000) High mobility of proteins in the mammalian cell nucleus. *Nature* 404:604–609.
2. Catez F, Brown DT, Misteli T, Bustin M (2002) Competition between histone H1 and HMGN proteins for chromatin binding sites. *EMBO Rep* 3:760–766.
3. Hendrix J, et al. (2011) The transcriptional co-activator LEDGF/p75 displays a dynamic scan-and-lock mechanism for chromatin tethering. *Nucleic Acids Res* 39:1310–1325.

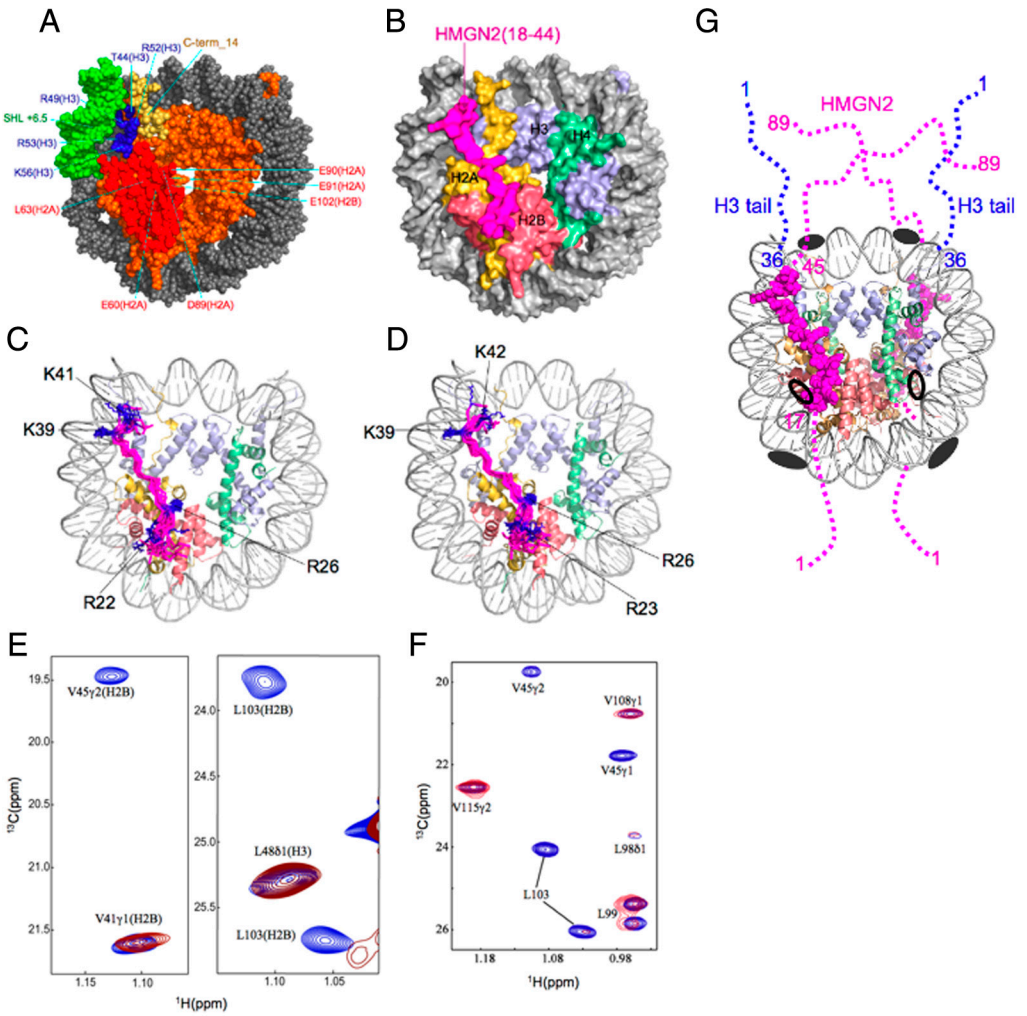

Fig. S6. *Computational modeling of the NBD-nucleosome complex using the docking program HADDOCK, the effect of binding of LANA (latency-associated nuclear antigen), and Interleukin-33 (IL-33) peptides on methyl groups Val45 and Leu103 in H2B in the nucleosome, and a model of the nucleosome complexed with HMGN2.* (*A*), Overview of the active residues in the nucleosome used in the docking calculation. The residues and nucleotides that were chosen as active residues are shown in red (histones H2A and H2B), blue (H3), and green (DNA). The residues in the C-terminal region in H2A are shown in yellow. Other residues in histones and nucleotides in DNA are shown in orange and dark gray, respectively. (*B*) Surface presentation of the complex, showing that the NBD fills the valleys on the surface of the nucleosome. (*C*), Distribution of the side chains of Arg22, Arg26, Lys39, and Lys41 in the cluster, showing that Arg26 and Lys39 have well converged conformation, whereas Arg22 and Lys41 are less well converged. (*D*) Distribution of side chains of Arg23, Arg26, Lys39, and Lys42 in the cluster, showing that Arg23 and Lys42 have less well converged conformation. Color coding: H2A, yellow; H2B, salmon red; H3, light blue; H4, light green; DNA, light gray; NBD, magenta. Arg and Lys residues are shown in blue sticks. Note that only one side of the nucleosome is shown. (*E*) Overlay of methyl-TROSY spectra of the free nucleosome (blue) and the LANA-bound nucleosome (red). Binding of the protonated LANA peptide to the acidic patch leads to severe attenuation of peak intensities for the Val45/L103 methyl groups in H2B. (*F*) Overlay of methyl-TROSY spectra of the free nucleosome (blue) and IL-33-bound nucleosomes (red). Binding of the IL-33 peptide, a homologue of LANA, results in similar changes in peak intensities and chemical shifts. Both LANA and IL-33 have been shown to bind to the acidic patch. The primary sequences of the two peptides are LANA—MAPPGMRLRSGRSTGAPLTRGS and IL-33—CPMYFMKLRSGLMIKKEA. (*G*) The NBD of HMGN2 is shown in magenta spheres. The unfolded terminal regions of HMGN2 and H3 are shown in dashed lines and indicated by the residue numbers. Color coding for the nucleosome core is light orange, H2A; light red, H2B; light blue, H3; light green, H4; light gray, DNA. The model was made by aligning the two H3 histones in two identical pdbs obtained from the docking calculation. This model is in general agreement with earlier protein photo-cross-linking studies with HMGN proteins in which specific residues were mutated to Cys, which showed that chemically modified residues 7 and 88 of HMGN1 (HMGN-14) are cross-linked with the N-terminal tail region (residues 25–66) of H2B (black open ovals) and with the N-terminal tail region (residues 20–50) of H3, respectively (1). In addition, chemically modified residue 28 of HMGN2 (HMGN-17) is also cross-linked to H3 (2). Moreover, binding of HMGN1 and HMGN2 to the nucleosome lead to marginal protection of the DNA from hydroxyl radical cleavage 25 base pairs from the end of the DNA in the nucleosome cores and in each of the two major grooves of the DNA flanking the nucleosomal dyad axis (black filled ovals) (3). Based on our model, these cross-linking results are likely due to the fact that the two terminal regions of HMGNs and the N-terminal tails of H3 have flexible conformations, which allow the cross-linked regions to interact transiently. Transient interactions between nucleosomal DNA and the flexible tails of the HMGNs may also be the cause for the marginal protections of DNA from hydroxyl radical cleavage. Alternatively, the protected regions of DNA may be stabilized indirectly by the binding of HMGN2 to the nucleosome (4).

1. Trieschmann L, Martin B, Bustin M (1998) The chromatin unfolding domain of chromosomal protein HMG-14 targets the N-terminal tail of histone H3 in nucleosomes. *Proc Natl Acad Sci USA* 95:5468–5473.
2. Ueda T, Catez F, Gerlitz G, Bustin M (2008) Delineation of the protein module that anchors HMGN proteins to nucleosomes in the chromatin of living cells. *Mol Cell Biol* 28:2872–2883.
3. Alfonso PJ, Crippa MP, Hayes JJ, Bustin M (1994) The footprint of chromosomal proteins HMG-14 and HMG-17 on chromatin subunits. *J Mol Biol* 236:189–198.
4. Roussel L, Erard M, Cayrol C, Girard JP (2008) Molecular mimicry between IL-33 and KSHV for attachment to chromatin through the H2H-H2B acidic patch. *EMBO Rep* 9:1006–1012.

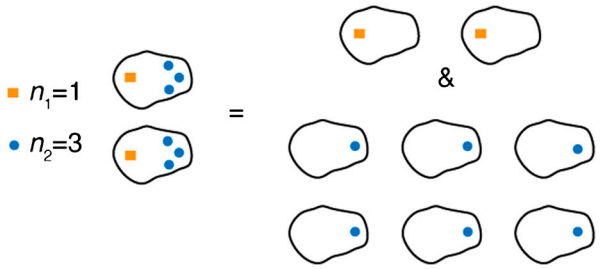

Scheme S1.

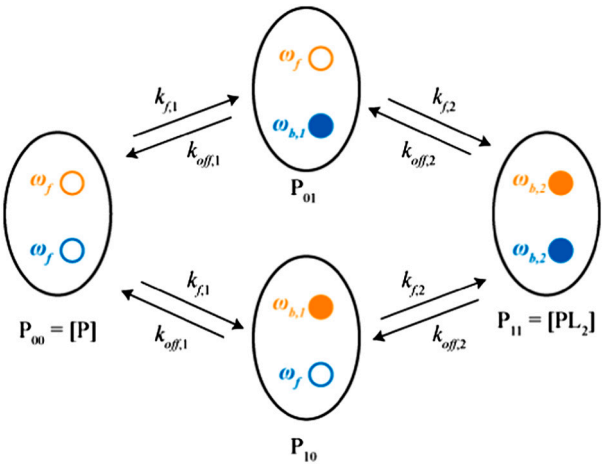

Scheme S2.

Table S1. Mutations for assigning the methyl groups in the nucleosome

I110V(H2A)/I74V(H3)	I86V(H2A)/I62V(H3)	I78V(H2A)/I124V(H3)
V53I(H2A)/L126I(H3)	L96I(H2A)/L100I(H3)	I29V(H2A)/I46V(H4)
V42I(H2A)/L49I(H4)	V61I(H2A)/L62I(H4)	L22I(H2A)/L97I(H4)
L33I(H2A)/V87I(H4)	L62I(H2A)/V60I(H4)	L92I(H2A)/V81I(H4)
L107I(H2A)/L42I(H2B)	L114I(H2A)/V57I(H4)	V48I(H2A)/L37I(H4)
L99I(H2B)/V70I(H4)	V41I(H2B)/L70I(H3)	I58V(H2B)/I51V(H3)
L98I(H2B)/L60I(H3)	L103I(H2B)/V46I(H3)	L97I(H2B)/V89I(H3)
V45I(H2B)/L82I(H3)	V108I(H2B)/L65I(H3)	L77I(H2B)/V117I(H3)
I91V(H2B)/I66V(H4)	I66V(H2B)/I29V(H4)	I36V(H2B)/I34V(H4)
V95I(H2B)/L92I(H3)	V115I(H2B)/V101I(H3)	C110A(H3)

I, Ile; L, Leu; V, Val.

Table S2. Methyl chemical shift assignment

H2A			H2B		
V9	CM2	21.045	I0	CD1	12.813
V9	QM2	0.944	I0	QD1	0.856
V9	CM1	20.412	I19	CD1	12.461
V9	QM1	0.929	I19	QD1	0.852
L22	CM1	26.866	I36	CD1	14.457
L22	QM1	0.789	I36	QD1	0.816
I29	CD1	13.538	I38	CD1	13.329
I29	QD1	0.995	I38	QD1	0.955
L32	CM1	25.306	V41	CG1	21.551
L32	CM2	21.943	V41	CG2	23.69
L32	QM1	0.534	V41	QG1	1.042
L32	QM2	0.805	V41	QG2	1.314
L33	CD1	25.606	L42	CD1	23.393
L33	CD2	23.038	L42	CD2	26.528
L33	QD1	0.712	L42	QD1	0.926
L33	QD2	0.481	L42	QD2	0.753
V42	CM1	21.299	V45	CG1	21.388
V42	CM2	22.448	V45	CG2	19.472
V42	QM1	0.921	V45	QG1	0.934

H2A			H2B		
V42	QM2	0.986	V45	QG2	1.075
V48	CM1	21.657	I51	CD1	12.978
V48	CM2	22.385	I51	QD1	0.71
V48	QM1	0.3	I58	CD1	14.417
V48	QM2	0.736	I58	QD1	0.983
L50	CD1	23.283	V63	CM1	22.845
L50	CD2	27.177	V63	CM2	21.763
L50	QD1	0.853	V63	QM1	0.526
L50	QD2	0.718	V63	QM2	1.045
V53	CM1	23.168	I66	CD1	8.814
V53	CM2	21.045	I66	QD1	0.547
V53	QM1	1.2	I70	CD1	13.723
V53	QM2	0.944	I70	QD1	0.623
L57	CM1	26.912	L77	CD1	27.083
L57	CM2	23.495	L77	CD2	24.69
L57	QM1	0.91	L77	QD1	0.599
L57	QM2	0.961	L77	QD2	0.6
L62	CD1	26.169	I86	CD1	13.598
L62	CD2	21.769	I86	QD1	0.693
L62	QD1	0.897	I91	CD1	7.171
L62	QD2	0.873	I91	QD1	0.34
L64	CD1	25.346	V95	CM1	23.213
L64	CD2	21.861	V95	CM2	25.134
L64	QD1	0.934	V95	QM1	1.074
L64	QD2	0.971	V95	QM2	1.199
I77	CD1	15.414	L97	CD1	26.138
I77	QD1	0.829	L97	CD2	22.441
I78	CD1	13.439	L97	QD1	0.45
I78	QD1	0.818	L97	QD2	0.538
L82	CD1	27.474	L98	CD1	26.209
L82	CD2	24.025	L98	CD2	24.453
L82	QD1	0.865	L98	QD1	0.81
L82	QD2	0.706	L98	QD2	0.859
L84	CD1	25.654	L99	CM1	25.502
L84	CD2	21.763	L99	CM2	25
L84	QD1	0.988	L99	QM1	0.925
L84	QD2	0.873	L99	QM2	0.925
I86	CD1	13.428	L103	CD1	25.621
I86	QD1	0.654	L103	CD2	23.776
L92	CD1	26.503	L103	QD1	1.007
L92	CD2	22.617	L103	QD2	1.049
L92	QD1	0.855	V108	CG1	20.438
L92	QD2	0.809	V108	CG2	22.45
L95	CD1	23.741	V108	QG1	0.936
L95	CD2	26.17	V108	QG2	1.149
L95	QD1	1.11	V115	CM1	22.189
L95	QD2	1.055	V115	CM2	24.342
L96	CD1	25.355	V115	QM1	1.165
L96	CD2	23.409	V115	QM2	1.289
L96	QD1	0.98			
L96	QD2	1.178			
V99	CM	20.873			
V99	CM1	19.28			
V99	CM2	20.872			
V99	QM	0.713			
V99	QM1	−0.001			
V99	QM2	0.713			
I101	CD1	11.717			
I101	QD1	0.78			
V106	CM1	22.01			
V106	CM2	18.051			
V106	QM1	0.921			
V106	QM2	0.963			
L107	CM1	24.255			
L107	CM2	24.84			
L107	QM1	0.864			
L107	QM2	0.881			
I110	CD1	13.439			
I110	QD1	0.818			
V113	CM1	20.175			
V113	CM2	20.546			
V113	QM1	1.042			

H2A			H2B		
V113	QM2	1.03			
L114	CD1	26.11			
L114	CD2	22.455			
L114	QD1	1.196			
L114	QD2	0.99			
L115	CD1	25.17			
L115	CD2	23.043			
L115	QD1	0.968			
L115	QD2	0.91			
H3			H4		
L20	CD1	24.812	I0	CD1	12.736
L20	CD2	23.4	I0	QD1	0.87
L20	QD1	0.94	L10	CD1	24.81
L20	QD2	0.885	L10	CD2	23.168
V35	CM1	20.197	L10	QD1	0.916
V35	CM2	20.931	L10	QD2	0.866
V35	QM1	0.906	V21	CM2	21.017
V35	QM2	0.906	V21	QM2	0.924
V46	CM1	21.55	V21a	CM1	20.513
V46	QM1	1.052	V21a	QM1	0.963
L48	CD1	25.271	V21b	CM1	20.44
L48	CD2	23.407	V21b	QM1	0.948
L48	QD1	1.044	L22	CD1	25.065
L48	QD2	0.943	L22	CD2	23.346
I51	CD1	13.184	L22	QD1	0.924
I51	QD1	0.643	L22	QD2	0.872
L60	CD1	25.907	I26	CD1	14.38
L60	CD2	21.389	I26	QD1	1.068
L60	QD1	0.864	I29	CD1	9.395
L60	QD2	0.755	I29	QD1	0.834
L61	CM1	24.119	I34	CD1	14.229
L61	CM2	23.634	I34	QD1	1.134
L61	QM1	0.586	L37	CM1	26.795
L61	QM2	0.742	L37	QM1	0.933
I62	CD1	13.307	V43	CM1	23.132
I62	QD1	0.925	V43	CM2	22.463
L65a	CM1	23.934	V43	QM1	0.759
L65a	CM2	24.921	V43	QM2	1.064
L65a	QM1	1.128	I46a	CD1	14.223
L65a	QM2	1.119	I46a	QD1	0.673
L65b	CM1	23.628	I46b	CM1	14.397
L65b	CM2	25.001	I46b	QM1	0.682
L65b	QM1	1.106	L49	CD1	25.13
L65b	QM2	1.112	L49	CD2	21.998
L70	CD1	22.867	L49	QD1	1.051
L70	CD2	26.768	L49	QD2	1.01
L70	QD1	0.786	I50	CD1	8.981
L70	QD2	0.72	I50	QD1	0.501
V71	CM1	21.445	V57	CM1	22.455
V71	QM1	0.28	V57	QM1	1.069
I74	CD1	14.946	L58	CD1	22.201
I74	QD1	0.843	L58	CD2	25.999
L82	CD1	26.826	L58	QD1	1.268
L82	CD2	23.854	L58	QD2	1.066
L82	QD1	0.873	V60	CM1	22.732
L82	QD2	0.765	V60	CM2	21.19
V89	CM1	22.149	V60	QM1	1.206
V89	CM2	22.647	V60	QM2	1.09
V89	QM1	0.977	L62	CM1	23.072
V89	QM2	1.183	L62	CM2	26.121
L92	CD1	26.042	L62	QM1	1.057
L92	CD2	25.153	L62	QM2	0.79
L92	QD1	0.978	I66	CD1	15.429
L92	QD2	0.904	I66	QD1	1.044
L100	CD1	26.533	V81	CM1	22.393
L100	CD2	22.307	V81	CM2	23.37
L100	QD1	0.911	V81	QM1	1.004
L100	QD2	0.708	V81	QM2	1.092
V101	CM1	24.009	V87	CM1	21.157
V101	CM2	21.771	V87	QM1	1.136
V101	QM1	1.266	L90	CM1	27.632
V101	QM2	0.887	L90	CM2	23.604

H2A			H2B		
L103	CD1	22.344	L90	QM1	0.888
L103	CD2	26.106	L90	QM2	1.018
L103	QD1	0.728	L97	CM1	28.424
L103	QD2	0.59	L97	QM1	0.882
L109	CD1	25.585			
L109	CD2	22.093			
L109	QD1	0.942			
L109	QD2	0.886			
I112	CD1	14.099			
I112	QD1	0.807			
V117	CM1	21.497			
V117	QM1	0.96			
I119	CD1	16.083			
I119	QD1	0.949			
I124	CD1	13.375			
I124	QD1	0.747			
L126	CD1	23.392			
L126	CD2	24.287			
L126	QD1	0.865			
L126	QD2	0.295			
I130	CD1	12.44			
I130	QD1	0.707			

Stereospecifically assigned methyl resonances are listed as QG1/QG2 (proton), CG1/CG2 (carbon) for Val and QD1/QD2 (proton), CD1/CD2 (carbon) for Leu; otherwise the two methyls are arbitrarily assigned as QM1/QM2 (proton) and CM1/CM2 (carbon).

Table S3. Effects of mutations on the binding between HMGN2 and the nucleosome

Mutant	K_D, μM	K_D(mutant)/K_D(wild type)
Wild type	0.089	
E60K (H2A)	ND	
E63K (H2A)	ND	
D89S/E(90,91)T (H2A)	ND	
E102T (H2B)	0.156	1.8
ΔC14 (H2A)	0.115	1.3
R22A (HMGN2)	ND	
R23A (HMGN2)	0.795	8.9
R26A (HMGN2)	ND	
S(24,28)E (HMGN2)	ND	
K(35,39,41,42)A (HMGN2)	0.445	5.0

ND, not determined.

K_D is the equilibrium dissociation constant obtained using model 2 to fit the ITC data, except for K(35,39,41,42)A mutant which was fitted to model 1.